SPE-173282-MS

Modeling of Magnetic Nanoparticle Transport in Shale Reservoirs

Cheng An, Masoud Alfi, Bicheng Yan, Kai Cheng, Zoya Heidari, and John E. Killough, Texas A&M University

This paper was prepared for presentation at the SPE Reservoir Simulation Symposium held in Houston, Texas, USA, 23–25 February 2015.

Abstract

Currently, the application of nanoparticles has attracted much attention due to the potential of nanotechnology to lead to revolutionary changes in the petroleum industry. The literature contains numerous references to the possible use of this technology for enhanced oil recovery, nano-scale sensors and subsurface mapping. Little work has been conducted to establish numerical models to investigate nanoparticle transport in reservoirs, and even less for shale reservoirs. Unlike conventional reservoirs, shale formations usually contain four pore systems: inorganic matter, organic matter dominated by hydrocarbon wettability, natural fractures and hydraulic fractures. Concurrently, hydraulic fractures and the associated stimulated reservoir volume (SRV) from induced fractures play a critical role in significantly increasing well productivity.

In this paper, a mathematical model for simulating nanoparticle transport in shale reservoirs was developed. The simulator includes contributions from Darcy flow, Brownian diffusion, gas diffusion and desorption, slippage flow, and capillary effects based on the extremely low permeability and micro- to nano-scale of the pores. Moreover, these diverse mechanisms are separately applied to different portions of the reservoir due to the variation in media properties. Applications of the model include numerical examples from two-dimensional micro models to macro models, both with organic matter randomly distributed within the inorganic matrix. The effects of varying water saturation, grid pressure, and mass concentration of nanoparticles are shown graphically in these numerical examples. The main conclusion from these models is that, as expected, nanoparticles can only easily flow along with the aqueous phase into the fractures, but their transport into the shale matrix is quite limited, with little transport shown into the organic matter. In addition, based on the measured properties of synthesized magnetic carbon-coated iron-oxide nanoparticles, the distribution of the volumetric magnetic susceptibility and the magnetization of reservoir including SRV are simulated and displayed in the numerical cases with and without magnetic nanoparticles. The results demonstrate that magnetic nanoparticles can effectively enlarge the magnetic susceptibility and the magnetization of reservoir thus producing enhanced signals from well logging devices such as Nuclear magnetic resonance (NMR) and leading to improved reservoir and fracture characterization. This simulator can provide the benefits of both numerically simulating the transport and distribution of nanoparticles in hydraulically fractured shale formations and supplying helpful guidelines for nanoparticles injection plans to enhance well logging signals. Furthermore, this model can also allow us to mimic the tracer transport flow in unconventional reservoirs.

Introduction

Shale reservoir is referred to as extraordinarily fine grained sediments with low porosity and extremely low permeability (Javadpour, 2009). As stated by Energy Information Administration, the shale gas will take up nearly half of the tradition gas supply by 2040. With the huge available resources and growing energy demand, shale reservoir has recently received significant interest and investigations. Hydraulic fracturing and horizontal drilling are two available necessary technologies which make shale gas become commercial producing. Wang and Reed (2009) proposed that the organic-rich shale reservoirs contains four pore systems: inorganic matter, organic matters with dominantly hydrocarbon wet, natural fractures and hydraulic fractures. Due to the organics can store methane as adsorbed gas and absorbed gas, shale gas is usually considered to exist in three forms: compressed gas in pores and fissures, adsorbed gas in the organic and inorganic matter, and dissolved gas in the kerogen (Javadpour 2009; Zhang et al. 2012). Meanwhile, taking into account of extremely low permeability and the micro and nano-scale of pore, some non-Darican mechanisms including gas diffusion, desorption and slippage flow have been considered to better explain the gas transport in shale reservoirs (Civan et al. 2011 and Shabro et al. 2012). Yan et al. (2013) established a two phase micro model in where mixed wettability, high capillary pressure and the kerogen randomly distributed are brought in to interpret the dynamic of gas and water flow at this micro scale level.

Currently, Development of nanotechnology has successfully offered technically and economically feasible alternatives for materials and technologies in many industries. Magnetic nanoparticles are a class of nanoparticles which could be manipulated using magnetic field and commonly consist of iron and their chemical compounds. With those advance revolution and potential advantages, application of nanoparticles have also attracted much attention and displayed numerous potential to lead evolutionary changes in petroleum industry, such as enhanced oil recovery, nano- scale sensors, drilling and completion. Typically, multiple transverse hydraulic fractures are created if the wellbore is design and drilled in the direction of minimum horizontal stress. Maximizing the total simulated reservoir volume (SRV) plays a critical role in the successful economical production from the unconventional gas reservoirs because it could increase the fractures conductivity and speed up the gas and liquid flow. In addition, modeling the gas flow process from the ultra-low permeability rock to the complex fracture network should be considered and conducted to effectively evaluate the stimulation design and completion strategies.

In spite of many applications of nanoparticles accomplished in petroleum industry, complex reservoir conditions such as high salinity, low permeability and porosity, and heterogeneous rock properties, still make nanotechnology challenging. The study of nanoparticles transport in porous medium is always one critical issue for both reservoir application and environmental concern. Few works have been completed to address the issue related to mathematical and numerical modeling of nanoparticles transport in porous medium. Ju et al. (2009) established a mathematical model of nanoparticles transport in two-phase flow in porous media based on the formulation of fine particles transport. El-Amin et al. (2012) also introduced a reservoir model to simulate the nanoparticles transport in porous media where mixed relative permeability, mixed-wet system and variations of both porosity and permeability are considered. Besides, Zhang (2012) has performed some core-flooding experiments and numerical simulation and compared this two results. However, to our knowledge, little work has been conducted with the nanoparticles transport in unconventional reservoirs such as shale reservoirs. The nanoparticles diameters are normally from 1 to 500 nm, which means Brownian diffusion need to be considered in the model. Moreover, various components of shale reservoir and complicated local flow mechanism make the model looking at the nanoparticles transport in shale reservoir more challenging. Therefore, an accurate mathematic model is required to be developed for better interpreting the transport process of particles based on the various flow physics and the interaction among different porous media.

This work is to develop a reservoir model for simulating the nanoparticles transport in water-gas flow in shale porous media. With dissimilar pore size, different flow physics including gas diffusion, desorption, slippage flow and Brownian diffusion are separately applied for the nonorganic matter, the organic matter and the fractures. Also the different connections between various pore media would be considered. For the nanoparticles flow, convection flow and Brownian diffusion are the dominant physics in fractures and matrix, where nanoparticle is only limited to flow within the water phase. Carbon-coated magnetic nanoparticles are chosen as model particles in our work because they have the great potential to enhance the logging signal and also possess remarkable future applications in magnetics, electronics, composite polymeric materials, and alternative energy. The work is mainly motivated by the application that the magnetic carbon nanoparticles could enhance the well logging signal by pumping them along with proppants into the fractures and reservoirs. To evaluate the connections between various porous media and clearly present the process of the nanoparticles transport, several numerical models are performed and shown as follows: 2D micro model with and without the organic matter, 2D macro model with and without the organic matter, and large reservoir model including stimulated reservoir volume. In addition, based on the measured properties of synthesized magnetic carbon-coated iron-oxide nanoparticles, the distribution of the volumetric magnetic susceptibility and magnetization of reservoir are computed and graphically displayed in the numerical cases with and without magnetic nanoparticles. The results demonstrate that magnetic nanoparticles could effectively enlarge the magnetic susceptibility and the magnetization of reservoir thus producing enhanced signals from well logging devices such as Nuclear magnetic Resonance (NMR), which leads to improved reservoir and fracture characterization. Moreover, these numerical results will be compared with some experimental data to validate the availability and effectiveness of this simulator.

Mathematical Modeling Description

In this paper, a mathematical model has been developed to describe the nanoparticles transport in two-phase (aqueous and gaseous) in shale reservoirs. The aqueous phase contains water and nanoparticles and the gaseous phase only includes natural gas methane. The water flow is mainly governed by the Darcy law, while the gas flow behaves differently because of extremely low permeability and micro and nano-scale of pores. Based on the Darcy's law, gas diffusion, gas desorption and slippage flow are also considered to explain the gas transport in shale reservoirs. Since the nanoparticles size used in this paper is about 30-80 nm which is small enough to consider strong Brownian motion, convection flow and Brownian diffusion are two major contributor for its transport. In order to study and investigate the transport mechanism of nanoparticles in fractured tight reservoirs, some assumptions are proposed to simplify and assist in the understanding of the complicated flow in shale reservoirs. Nanoparticles only transport in the aqueous phase, which means it cannot flow into the gaseous phase. Additionally, the interaction between nanoparticles and reservoir matrix is ignored, and nanoparticle deposition is not significant.

Three main mass balance equations about water, gas and nanoparticles, are applied to solve the unknown variables with the effective Newton-Raphson iteration in this mathematical model as below. These continuum equations are also discretized in space using the integral finite difference method. All the numerical cases are performed under isothermal environment in this paper, so the heat transfer and loss are neglected.

$$\frac{\partial}{\partial t} M_l = \nabla \cdot \left(\overrightarrow{F_l}\right) + \sum Q_l \tag{1}$$

$$\frac{\partial(\phi S_w C)}{\partial t} + \nabla \cdot (C\overrightarrow{v_w}) = \nabla \cdot (D_e \nabla C) + \sum Q_{Nano} \tag{2}$$

Where ***l*** denotes the index of component, water or gas, M_l indicates the mass accumulation of component ***I***, $\boldsymbol{F_l}$ represents the flux of component ***I***, $\boldsymbol{Q_l}$ stands for source or sink of component ***I***, C denotes

concentration of nanoparticles, $\boldsymbol{Q_{Nano}}$ indicates the source or sink of nanoparticles, $\boldsymbol{D_e}$ represents the diffusion coefficient of nanoparticles which is obtained from the modification of stokes-Einstein's Equation (6) (Millington and Quirk 1961). To better explain these mass balance equations above, more equations from (3) to (6) with more detail are presented.

$$M^l = \sum_\beta \phi S_\beta \rho_\beta X_\beta^l \tag{3}$$

$$\overrightarrow{F_A^l} = -\rho_A k \frac{k_{rA}}{\mu_A}(\nabla P + P_c - \rho_A \vec{g}) X_\beta^l \tag{4}$$

$$\overrightarrow{F_G^l} = -\rho_G k \frac{k_{rG}}{\mu_G}\left(1 + \frac{b}{P}\right)(\nabla P + P_c - \rho_G \vec{g}) X_\beta^l \tag{5}$$

$$D_e = \frac{K_B T}{3\pi \mu_w d_p} \phi^{\frac{3}{4}} S_w^{\frac{10}{3}} \tag{6}$$

Where β denotes the index of fluid phase (A is aqueous phase and G is gaseous phase), ϕ indicates the porosity of porous media, S_β represents the saturation of phase β, p_β stands for the density of phase β, X_β^l denotes the mass fraction of component l in the phase β, k indicates the absolute permeability of porous media, $k_{r\beta}$ represents the relative permeability of phase β, μ_β stands for the viscosity of phase β, P_c denotes the capillary pressure, b indicates the Klinkenberg factor accounting for gas slippage effects, K_B represents the Boltzman constant, T stands for the absolute temperature, μ_w denotes water viscosity, d_p indicates the diameter of nanoparticles.

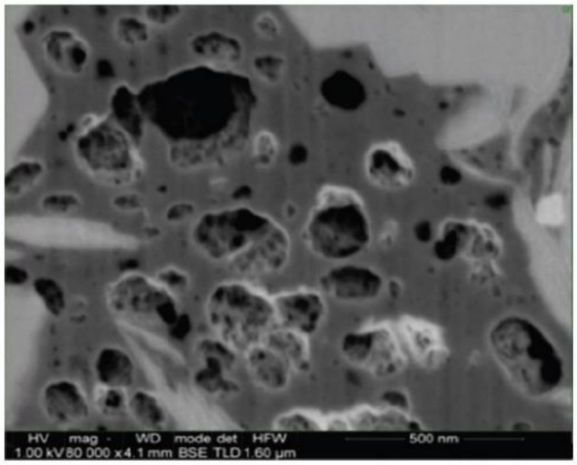

Figure 1—Local pore distribution in kerogen, smaller pores reside on the wall of large pores (Curtis et al. 2010).

Figure 2—3D SEM segmentation showing kerogen network, yellow outlines the kerogen network (Ambrose et al. 2010).

Substituting the equations above into the governing Equation (1), a set of first order ordinary differential equations in time is obtained as Equation (7). Using the fully implicit, time is discretized as a first-order finite difference and the flux and sink and source terms are evaluated at the new time level $t + 1$. Each gird block includes three equations in this paper, so that for a mesh discretized into N grid blocks, Equation (8) represents a total of $3 \times N$ coupled non-linear equations. To solve them, Newton Raphson iteration is computed and continued until the residuals $R_n^{k,t+1}$ is smaller than a present convergence tolerance. If convergence cannot be achieved within a certain number of iterations, the time step size Δt will be reduced and a new iteration process is started.

$$\frac{dM_n^k}{dt} = \frac{1}{V_n}\sum_m A_{nm} F_{nm}^k + q_n^k \tag{7}$$

$$R_n^{k,t+1} = M_n^{k,t+1} - M_n^{k,t} - \frac{\Delta t}{V_n}\left(\sum_m A_{nm} F_{nm}^{k,t+1} + V_n q_n^{k,t+1}\right) = 0 \tag{8}$$

Where $R_n^{k,t+1}$ denotes residuals, superscript k indicates component index (water, gas, and nanoparticle), superscript t represents the previous time step, V_n denotes volume of grid n, A_{nm} indicates interface between grid n and m, $t + 1$ stands for the current time step.

Micro Model Description and Results Analysis

With the advantages of advanced analytical tools, such as scanning electron microscope (SEM), kerogen matter has been found to be widely scattered in many shale reservoirs, such as Eagle Ford, Woodland, and Bakken. Moreover, the presence of kerogen could provide more available hydrocarbon sources, improve matrix porosity, alter grain density and wettability, and bring in various flow mechanisms in shale reservoirs (Curtis et al. 2012 and Ambrose et al. 2010). Fig. 1 shows large and small pores in kerogen matter, and Fig. 2 presents the kerogen network in the 3D SEM image. As we discussed above, the shale reservoirs usually contain organic matter, inorganic matter, and fractures, so subdividing the shale matrix into the inorganic matter and the organic matter with different pore geometries could better describe and explain the diverse connections between them and capture different flow mechanisms between various pore systems. Characterized as high permeability, natural fractures act as pathways to connect shale matrix blocks with the induced fractures network and the well bore. Besides, for all the numerical models in this paper, the kerogen matter is randomly distributed in the matrix and their abundance is directly related to the properties of each medium and the Total Organic Carbon (TOC) content in the Equation (9) (Yan et al. 2013). The inorganic matter is regarded as water-wet while the kerogen matter is considered to be hydrocarbon-wet in our models, which could produce some differences about capillary pressure and relative permeability on various pore medium. For example, the mobile water pressure is smaller to its grid pressure in the inorganic matter because of capillary pressure effect, while it is equal to its grid pressure in the kerogen matter grids.

$$TOC = \frac{\rho_{krg} N_{krg} (1-\phi_{krg})}{\rho_{krg} N_{krg} (1-\phi_{krg}) + \rho_{inorg} N_{inorg} (1-\phi_{inorg})} \times 100\ wt\% \tag{9}$$

Where p_{krg} denotes the density of the kerogen matter, N_{krg} means the number of kerogen grids in the mesh, ϕ_{krg} indicates the porosity of the kerogen matter in the shale matrix, p_{inorg} stands for the density of the inorganic matter, N_{inorg} represents the number of inorganic grids in the mesh, ϕ_{inorg} denotes the porosity of the inorganic matter in the shale matrix.

In our numerical simulator, two phase flow carrying nanoparticles will be modeled in different pores systems. As the mean free path of gas molecules become small enough, the interaction between molecules and rock surface will play an important effect in addition to the viscous flow. Therefore, diffusive flow has to be considered based on the micro-scale and nano-scale pores size. Different with conventional gas reservoirs, the gas storage mechanism is involved with compressed gas and adsorbed gas. As pressure decreases, adsorbed gas in the kerogen will be gradually desorbed as free gas, which actually increase the gas accumulation and production in organic shale reservoirs. In this paper, the Brooks and Corey formulations are applied for capillary pressure calculations, and Fig. 3 shows the two-phase relative permeability curves along with the changing of wetting phase saturation.

In this section, the 2D micro models are built and performed to mimic the dynamic flow of water, nanoparticles, and gas in shale matrix and fractures. The 2D micro models include 12×12 grids and the size of each grid for X, Y, and Z are $1 \times 10^{-5}\ m$,$1 \times 10^{-5}\ m$, *and* $1 \times 10^{-5}\ m$. The shale matrix contains 10×10 grids, which is surrounded by the fractures. To investigate the influence of the kerogen matter on the nanoparticles transport, two different 2D micro models are conducted and compared: one contains the kerogen matter and the other one does not. In the Fig. 4, the left graph only contains the inorganic matter and fractures, where the blue color grids represent the inorganic matter and the red color of outside surrounding grids stand for the fracture media. The right graph of Fig. 4 includes inorganic matter, organic matter, and fractures. The light green grids represent the organic matter, where 15% organic matter (15 grids) are randomly distributed among the shale matrix. One random function program is used to achieve the goal of random distribution of organic matter.

The main media parameters for the 2D micro models are shown in Table 1. The fracture media has higher pressure, higher porosity and permeability, and higher nanoparticles concentration than the

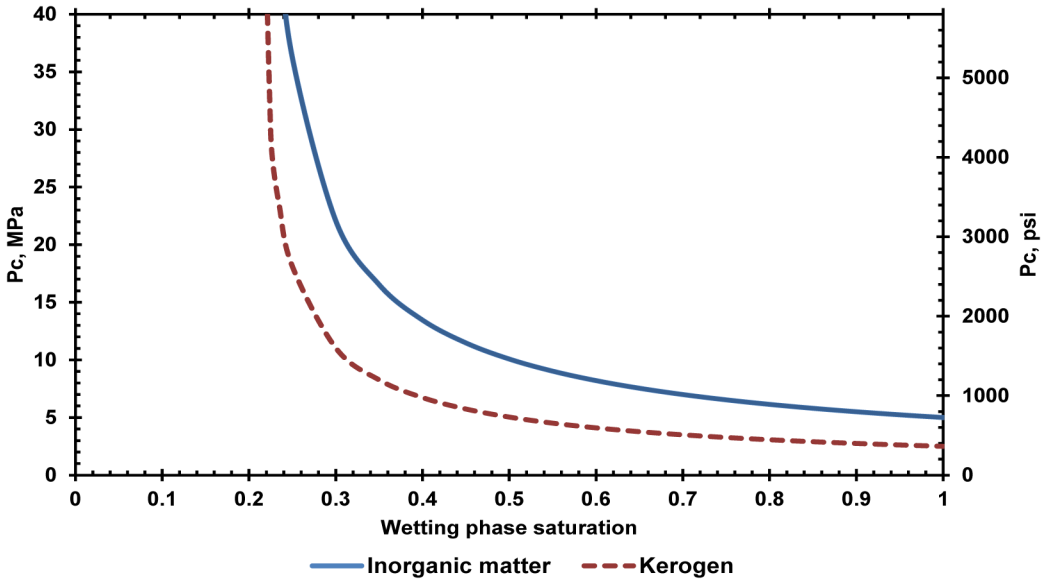

Figure 3—Capillary pressure vs. wetting phase saturation for Inorganic matter and Kerogen matter.

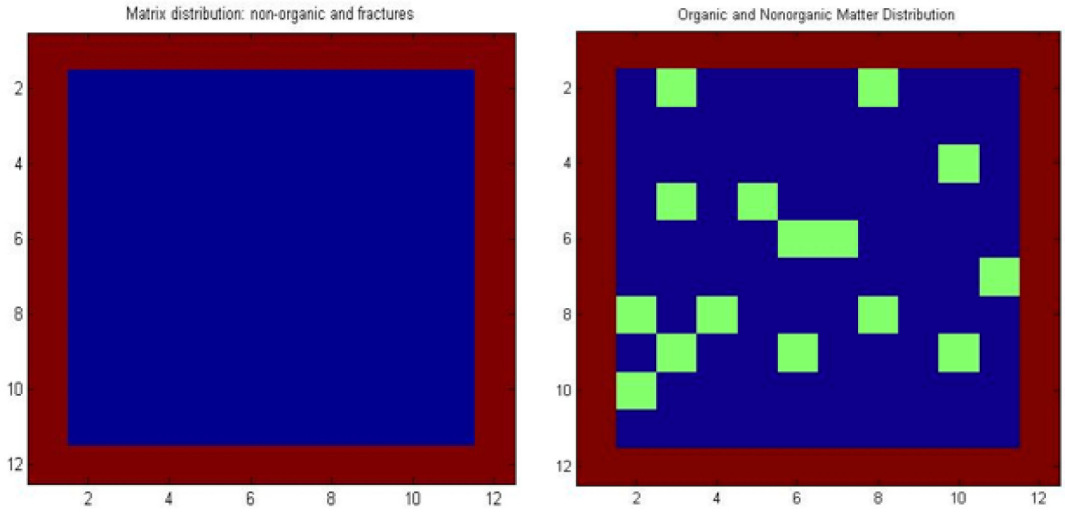

Figure 4—The distribution of nonorganic, organic matter and fracture in 2D micro shale matrix.

inorganic matter and organic matter. We focus on large pore space in the kerogen, and diffusivity is only considered in the organic matter. Different with inorganic matter, the initial water saturation of organic matter is only 0.01, because organic matter is hydrocarbon-wet and no irreducible water saturation exists on the pore surface. Mass concentration of nanoparticles are used as indicator to show the changing trend of nanoparticles, which is computed as below.

$$m_{NPs} = C_i \times \phi_i \times (S_w)_i \times Vol_i \tag{10}$$

Where m_{NPs} denotes the mass of nanoparticles, C_i represents the concentration of nanoparticles, ϕ_i indicates the porosity of the pore media, S_w stands for the water saturation, Vol_i denotes the volume of the grid.

In this 2D micro model, water is flowing from the fractures into the matrix and gas is drained out from the matrix, because the fracture grids hold the higher pressure and water saturation than the matrix. In the Fig. 5 and 6, the changing trend of water saturation and mass concentration of nanoparticles is displayed in a time sequence, from the early time to the final time. In the micro model with only non-organic matter,

Table 1—Main parameters for the pore media in the 2D micro models

Table 1: Main parameters for the pore media in the 2D micro models

Pore Medium	Fracture	Inorganic	Organic
Density, kg/m^3	--	2.6×10^3	1.35×10^3
Porosity	1.0	0.02	0.2
Permeability	84 mD	50 nD	50 nD
Diffusivity, m^2/s	--	--	8.21×10^{-5}
Pressure, Pa	2.72×10^7	1.72×10^7	1.72×10^7
Water Saturation	0.99	0.21	0.01
NPs Concentration, kg/L	1.0×10^{-6}	1.0×10^{-20}	1.0×10^{-20}
Temperature, ℃	100	100	100

nanoparticles are flowing into the shale matrix along with water phase and obviously they (water and nanoparticle) have the similar varying pattern in the Fig. 5. The numbers of X and Y axes on the Fig. 5 and 6 represent the grid number, from first grid to twelfth grid. Actually most nanoparticles entered the matrix at only about 2.4 seconds because of micro size scale, while it takes about 1.29×10^2 seconds to achieve the steady status. The pressure finally reaches equal between the fracture grids and middle matrix grids. The water saturation and nanoparticles concentration also reach equal and stable at the final time stages, which means the water and nanoparticles enter all the matrix.

However, the dynamic flow in the micro model including organic matter is different with the model with only non-organic matter even though at the same initial condition. 15% of organic matter is randomly distributed among the matrix as mentioned, some of which are connected with the surrounding fractures and others are only connected with the non-organic grids, as in the right graphs of Fig. 4. Different from the non-organic matter, gas is considered as wetting phase in the organic matter, so capillary pressure effect only works on the gas phase in these organic grids. For these organic grids connected with the fracture, the water phase pressure is keeping increasing because of the invasion of water from the fractures and is eventually equivalent with the fractures pressure which means no more water flow in after that. Furthermore, some gas could also flow out from these organic grids while not too much because of high capillary pressure for gas phase. For these organic grids only connected with non-organic grids, water could flow in from these non-organic grids with higher pressure and water saturation, while it is limited because of high capillary pressure for water phase in the non-organic grids. For these non-organic grids in matrix, water is flowing into and gas is flowing out in the similar way with the non-organic grids. However, more water could flow into these non-organic grids from the fractures because its mobile water pressure is reduced by high capillary effect. In other words, if water phase want flow out from the non-organic grid, it has to overcome the capillary pressure. So the mobile water pressure of non-organic gird is smaller than that of organic grids even though both grids pressure finally reach equal with the pressure of fracture grids. Therefore, non-organic grids receive more water inflow than organic grids connected with the fracture, and the organic grids connected with fractures obtain more water inflow than these organic grids only connected with non-organic grids.

As seen from the early time to final time on the Fig. 6, water and nanoparticles are gradually flowing into the matrix, and performing differently in non-organic and organic grids as we analyzed above. In the

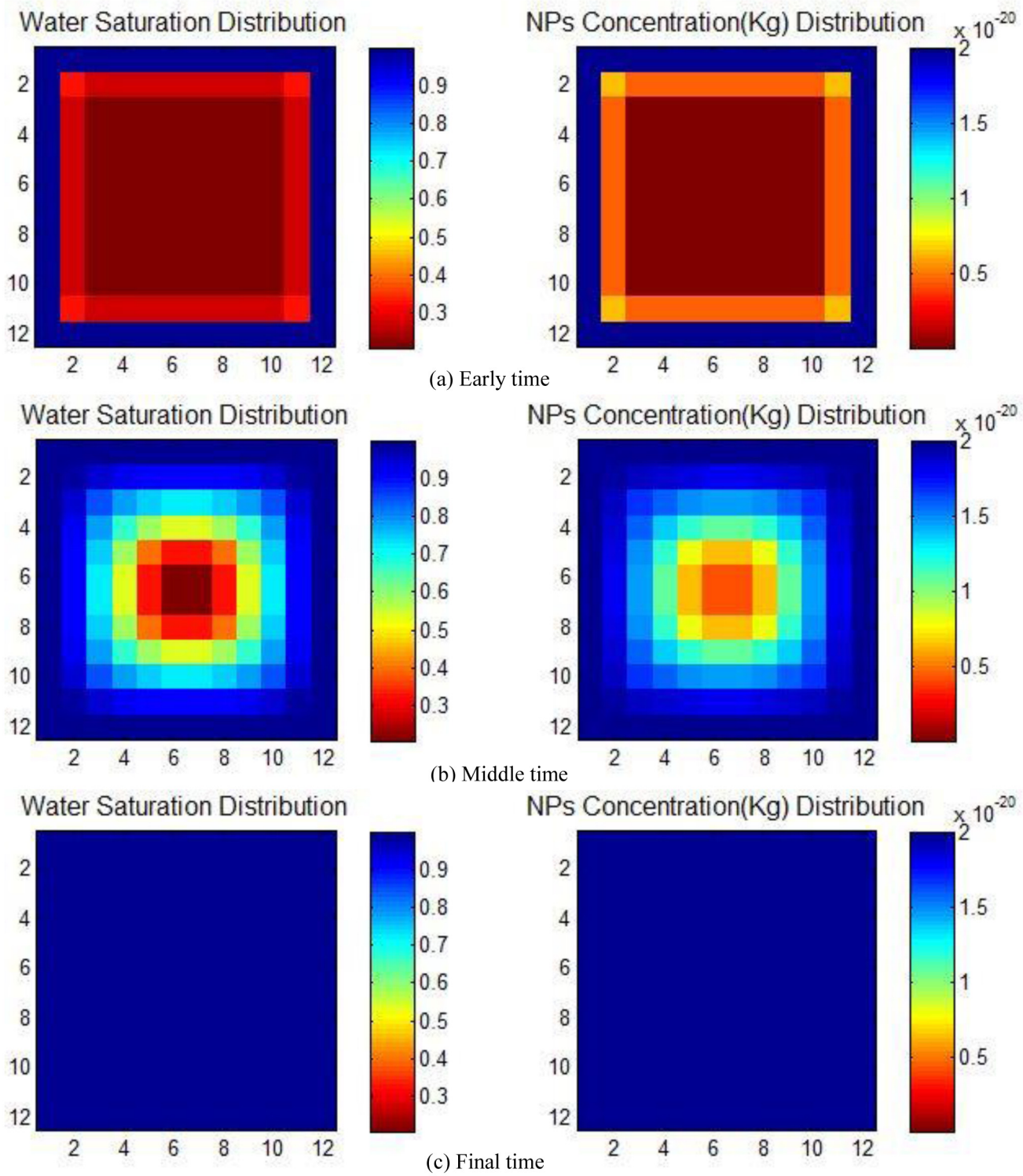

Figure 5—The distribution of water saturation and nanoparticles concentration at different time steps in the 2D micro model without organic matter.

right graphs of Fig. 6, nanoparticle has a similar flow model with the water phase into the matrix, where it is easily to flow into the non-organic grids while restricted for the organic grids. In spite of that, the distribution of nanoparticle mass concentration is dissimilar with the distribution of water saturation. Due to the porosity of organic matter is ten times larger than that of the non-organic grids, the mass of nanoparticles in these organic grids which share the high fracture permeability by directly connecting with

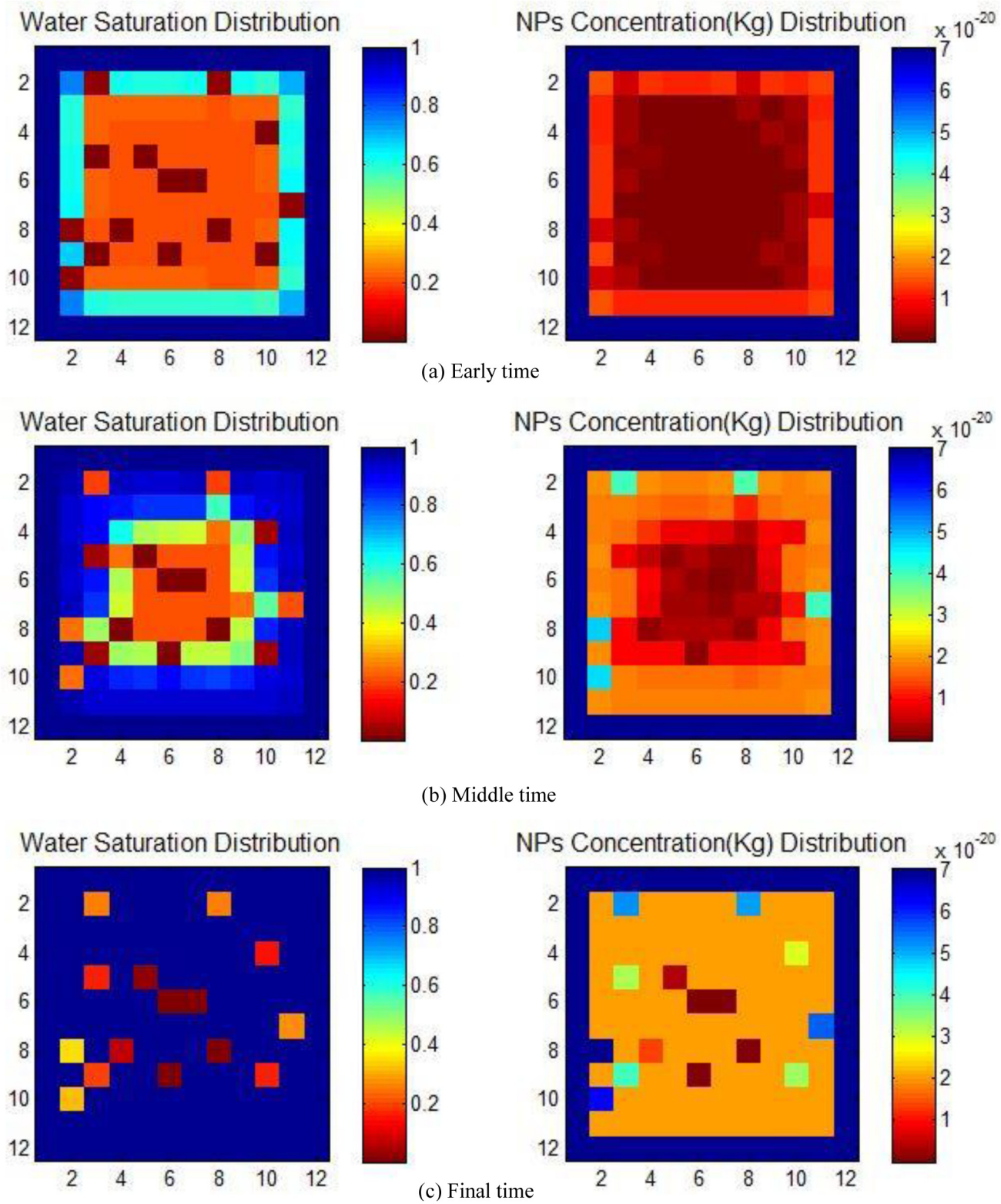

Figure 6—The distribution of water saturation and nanoparticles concentration at different time steps in the 2D micro model with organic matter.

the fracture grids, is bigger than that of non-organic grids although the non-organic grids contain higher water saturation, as computed with Equation (10). However, as shown in the part (c) of Fig. 6, most organic girds only connected with non-organic grids, merely obtain little improvement on water saturation

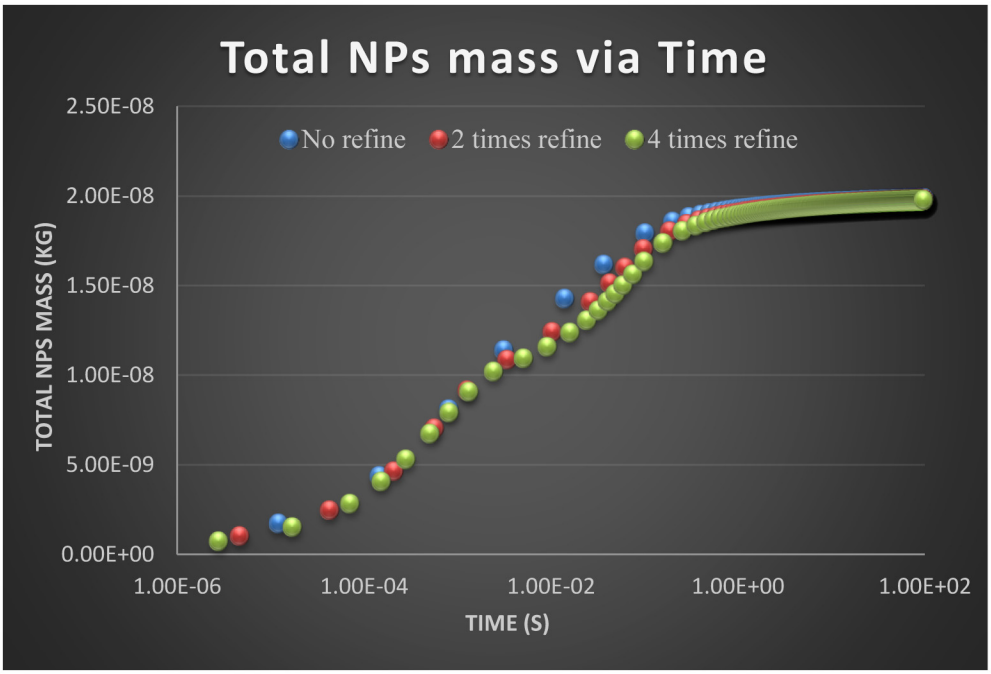

Figure 7—Total nanoparticles mass along with time in the micro models without organic matter.

and mass of nanoparticles. For example, water saturation is improved from 0.01 to 0.02 in one organic grid.

The plots about total nanoparticles mass along with time are shown for the micro modes without organic matter in Fig. 7. After the nanoparticles mass in each grid was calculated by using Equation (10), we sum up all the matrix grids to get the total mass of nanoparticles in matrix. As you could see, the total mass of nanoparticles goes up along with time and reach stable status at the last stage. In other words, the nanoparticles are gradually flowing into the matrix until it cannot enter the matrix any more. This plot could mainly tell two key information: one is how much nanoparticles in total could flow into the matrix, other is how long the process takes. The curves show all the nanoparticles enter the matrix in a very short time for the micro model while it needs much longer to reach convergent status. Because of tiny grid scale, this micro model took about one second to reach stable status, while it took about two minutes for the simulator achieving convergent status. To verify and confirm the results, we refined the shale matrix into two times and four times, where two times refine means one grids is refined into four equal smaller grids. As usually, the smaller gird and mesh could provide more accurate results. As shown on Fig. 7, the basic matrix without refining and the refined matrix provide the almost same result for the variation of the total nanoparticles mass along the time, which confirmed the numerical results we obtained from the basic model. Of course, the refined mesh always needs more computation and takes longer time to perform.

Brownian diffusion and convection flow are two flow mechanisms for the transport of nanoparticles. To investigate the effect of nanoparticles diffusion and how much it contributes to the total nanoparticle movement, we performed two micro models including organic matter with and without nanoparticle diffusion. As the Fig. 8, the blue curve presents the model where diffusion of nanoparticles is considered and the red curve does not take into account the diffusion. Clearly the blue curve has large total mass of nanoparticles invaded into the matrix than the red curve because it has two flow contributions. In the both models, the total mass of nanoparticles are rapidly increasing along the time and reach stable status at the later stage. After comparing this two models, we found the Brownian diffusion contributes about 18% of the entire transport of nanoparticles in Equation (11). In other words, the convection flow is the major flow mechanism for nanoparticles.

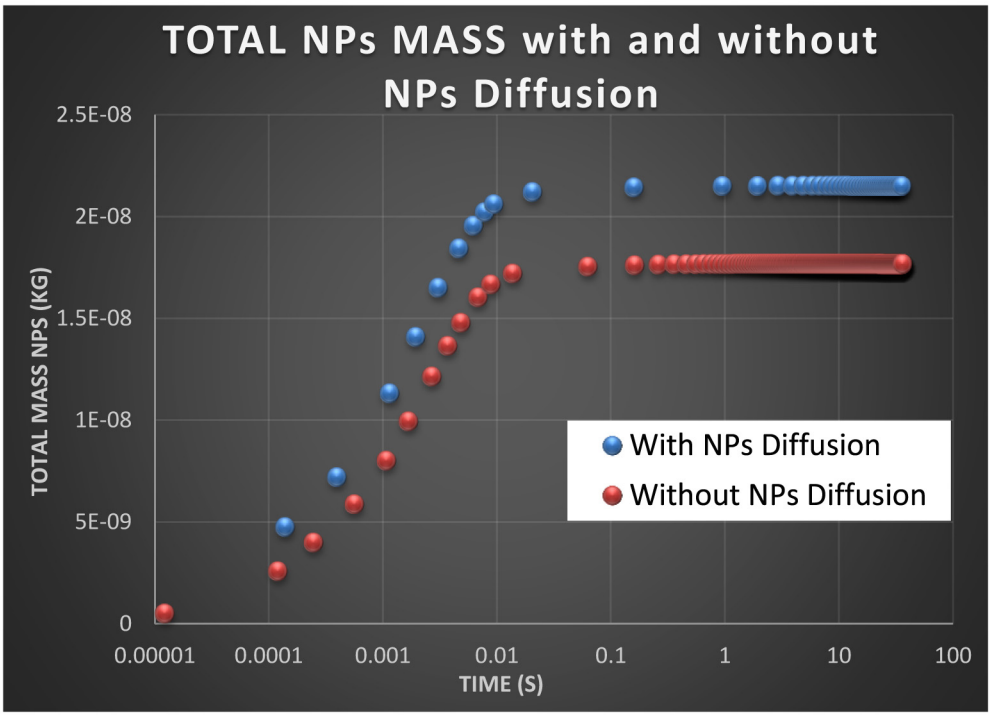

Figure 8—Total mass of nanoparticles for 2D micro models including organic matter with and without nanoparticles diffusion.

$$\frac{With\_Diff - Without\_Diff}{With\_Diff} = \frac{2.148\times10^{-8} - 1.766\times10^{-8}}{2.148\times10^{-8}} = 18\% \tag{11}$$

Overall, based on the results from the micro models with and without organic matter, we could found that water and nanoparticles can quickly flow into the non-organic grids, while it is hard and restricted to flow into the organic matter if they are not connected with the fracture grids. In other words, it is limited to flow from the non-organic matter or organic matter to the organic matter in our models. Moreover, the major invasion of water phase and nanoparticles into the matrix could be completed in an extremely short time. The Brownian diffusion mechanism contributes about 18% to the entire transport of nanoparticle in the models.

Macro Model Description and Results Analysis

In the 2D micro models, the water and nanoparticles could flow into all the matrix because of tiny scale. To investigate how far these nanoparticles could flow into the matrix on the same initial condition, the 2D macro models have been built. Same with micro model, the mesh of macro model contains identical 12 $\times$ 12 $\times$ 1 girds which include inorganic matter, organic matter, and the fracture. The grid size of X, Y and Z are enlarged from 1×10^{-5} m of micro size to 1×10^{-1} m of macro size, while all the other reservoir properties and grids structure keep the same, just the same with the Table 1. With the large grid size, flowing through one grid will take longer time and the mass of nanoparticle in grid will also rise because of large grid volume. Two macro models with and without organic matter are displayed and the distribution trend of water saturation and mass concentration of nanoparticles are also shown in a time sequence. As the same with micro models, 15% organic matter (15 grids) is randomly dispersed among the matrix on the macro model, and the mass concentration of nanoparticles computed by Equation (10) is still used as indicator to show the changes of nanoparticles.

In the 2D macro model without organic matter, the water is flowing into the matrix and gas is drained out due to the pressure and nanoparticle concentration gradient between surrounding fractures and middle matrix. As shown from the early time to final time in the Fig. 9, water phase and nanoparticles are

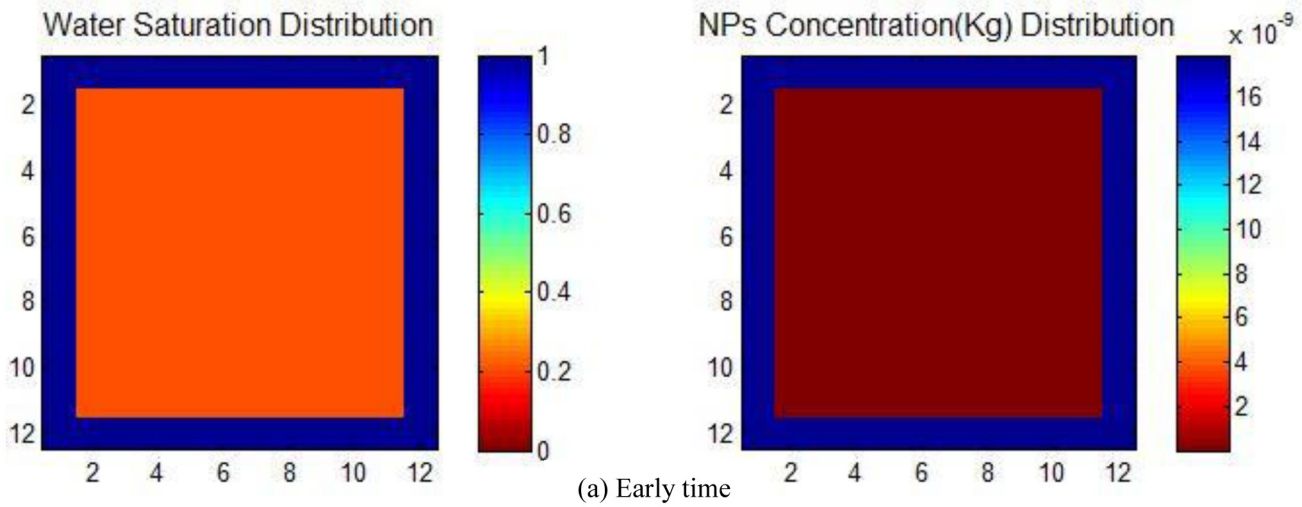

(a) Early time

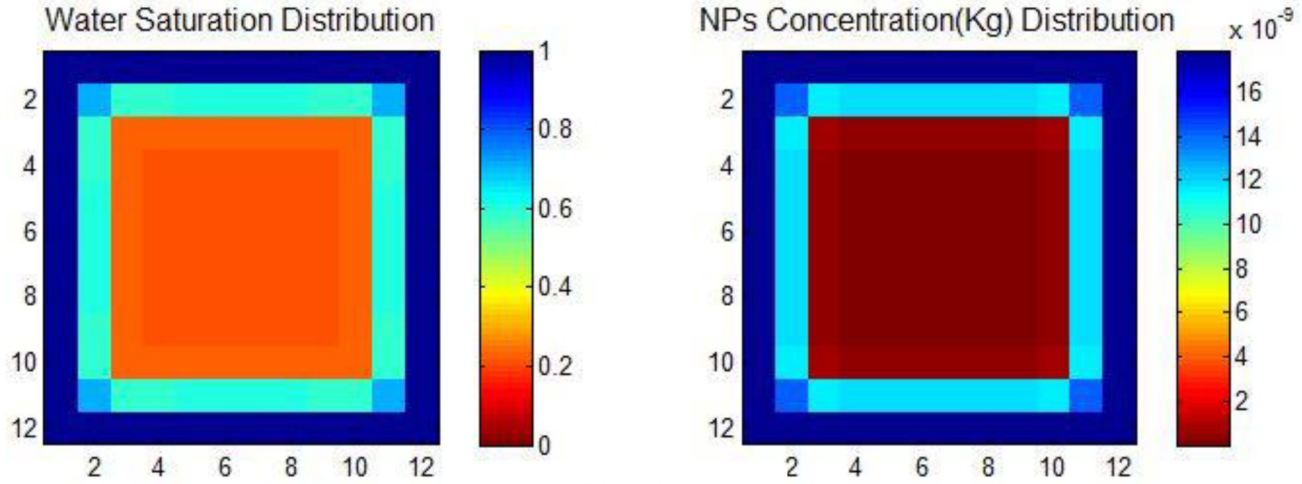

(b) Middle time

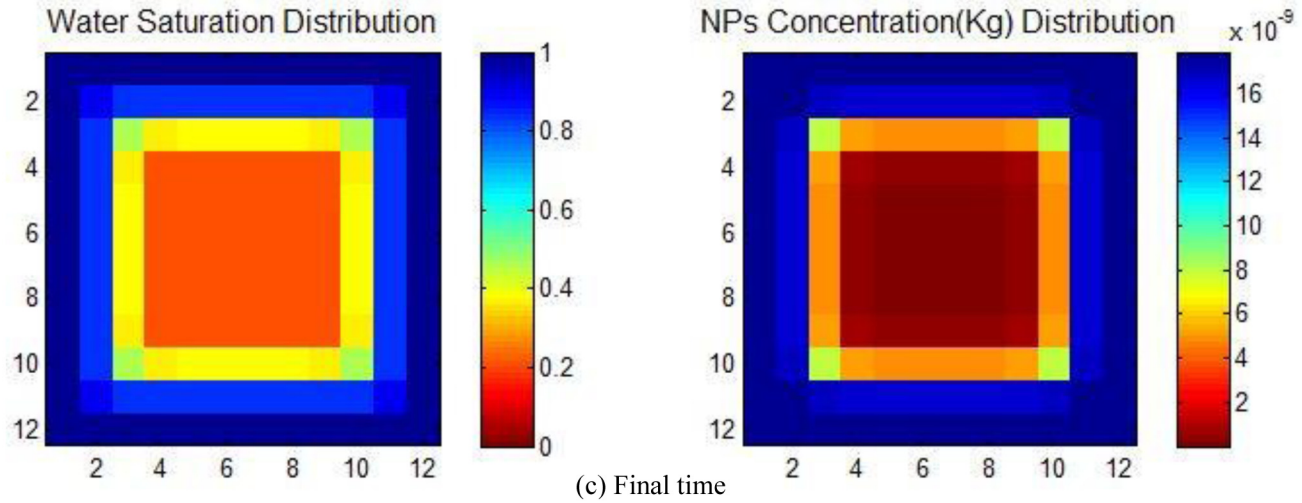

(c) Final time

Figure 9—The distribution of water saturation and nanoparticles concentration at different time steps in the 2D MACRO model without organic matter.

gradually flow into the matrix and they have the similar changing trend. However, the water and nanoparticles could only invade two grid blocks into the matrix, about 20 centimeters distance, before the simulator reaches convergence and stable. In other words, the nanoparticles cannot flow into the matrix any further.

If we do not count the fracture grids and only count matrix grids from outside to inside, the water saturation of first surrounding matrix grids reaches about 0.84 and its pressure is even bigger than the fractures pressure at the final time stage. All the pressure in this paper means the wetting phase pressure of the grid. Since water is wetting phase in non-organic grids and a big capillary pressure effect on the water movement, the fracture grids and the first surrounding matrix grids could still have equal water mobile pressure, even though the first surrounding matrix grids have higher pressure than the fractures. In addition, gas phase has a very low relative permeability when the water saturation (wetting phase) is bigger than 0.8, so basically the left gas phase of the grids cannot flow out. For the second surrounding matrix grids, some water and nanoparticles are flowing from the first surrounding matrix grids into them to increase its water saturation and nanoparticles. At the final time stage, the water saturation of second surrounding grids arrive at about 0.38 and water saturation of the rest of matrix grids increased a little bit. The distribution of nanoparticles mass concentration is very similar with water saturation. As the right graphs of Fig. 9, the nanoparticle could only enter the matrix about two grid blocks. The second surrounding matrix grids did not even reach a high nanoparticles mass concentration like the first surrounding matrix grids, and the third surrounding matrix grids only increased a little on the mass concentration of nanoparticle.

Looking into the 2D macro model with organic matter, the changing trend of water saturation and nanoparticles concentration is shown in Fig. 10. From the early time to final time in Fig. 10, water phase are easy to flow into the non-organic grids while experiencing difficulty to enter all organic grids. Besides, these organic grids connected with the fractures have higher water saturation than other organic grids. Same with previous macro model without organic matter, the water and nanoparticles could only invade about two grid blocks into the matrix, about 20 centimeters distance. Even though little water and nanoparticles also flowed into the third surrounding matrix grids, there is an obvious gradient for water saturation and nanoparticle concentration. In addition, these organic grids connected with the fractures contain more nanoparticles than the non-organic grids, because their grids volume is much bigger as we explained in the micro model. But to be clear, the mass nanoparticles of non-organic grids is larger than most organic girds, as presented in the last time of Fig. 10.

The most important information we could obtain from macro models is that water phase and nanoparticles could only flow into shale matrix with very limited distance. Besides, compared to the long time to reach the convergent and stable status for the simulator, the majority invasion of water and nanoparticle could be completed in a short time.

Reservoir Model Description and Results Analysis

Horizontal drilling and hydraulic fracturing are two necessary techniques to economically produce oil & gas from extra-low permeability reservoir. Fracture direction is most influenced by the formation stresses, while it could be also be modified by the fracture design, such as the treatment pressure and volume. Typically, multiple transverse hydraulic fractures could be created if the wellbore is design and drilled in the direction of minimum horizontal stress. Complex-fracture networks could improve the fracture surface contact area with the shale through both size and fracture space. The concept of stimulated reservoir volume (SRV) was developed by Fisher at al. (2004) to provide some quantitative measure of stimulation effectiveness in the Barnett shale based on the size of the microseismic images. Various types of fracture growth including simple fractures and complex fracture network are display in Fig. 11. Secondary fractures are often generated along with the changed condition of the fracture design, which in return increases the area of the flow path and fracture conductivity. Moreover, some secondary fractures have

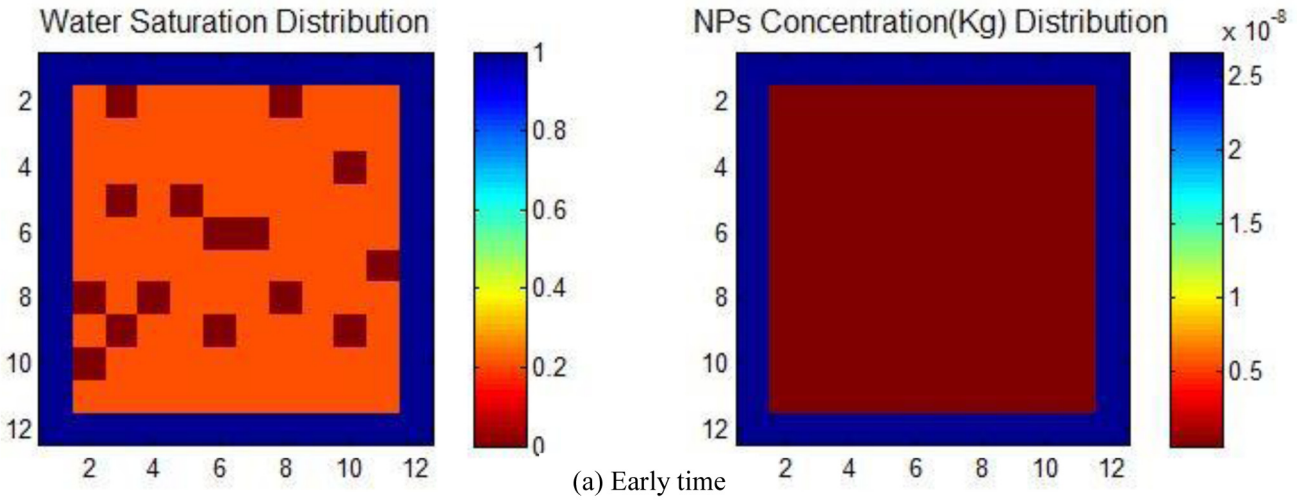

(a) Early time

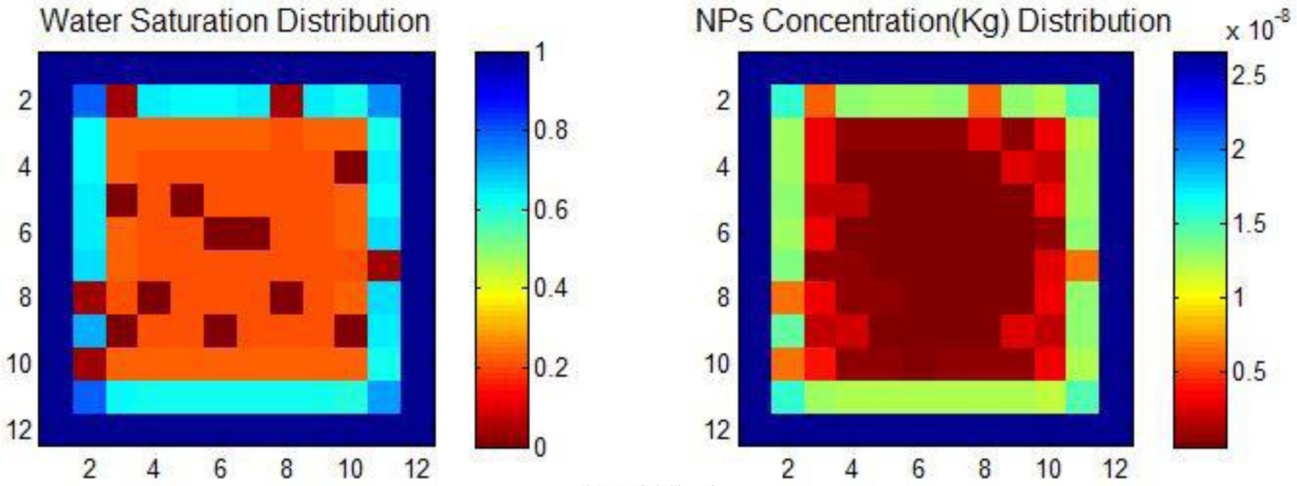

(b) Middle time

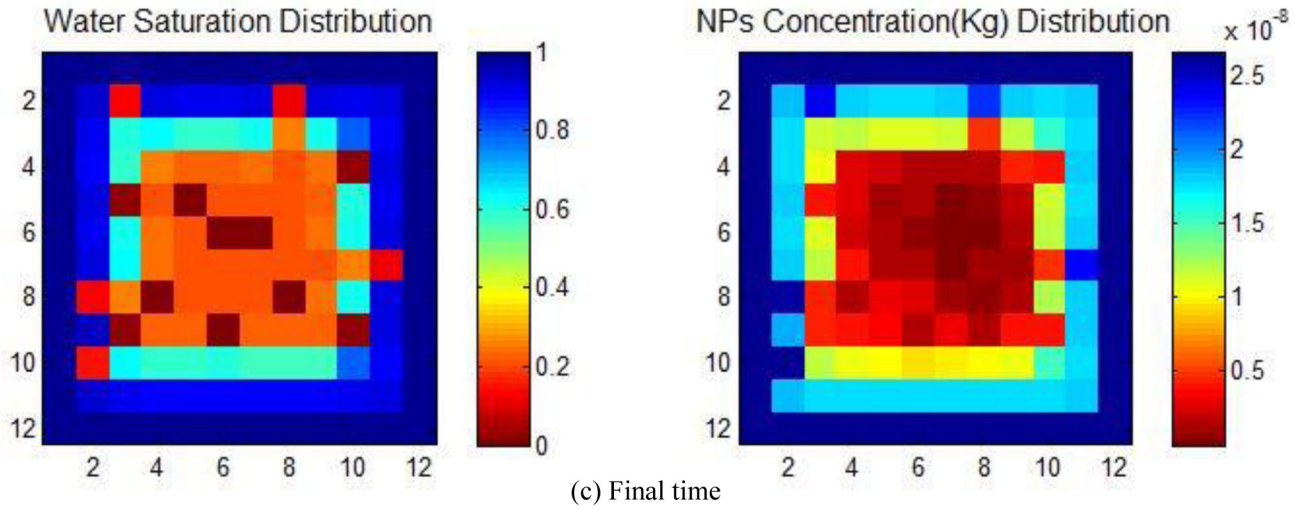

(c) Final time

Figure 10—The distribution of water saturation and nanoparticles concentration at different time steps in the 2D MACRO model with organic matter.

been found in micro-seismic events and outcrops. King et al. (2008) have presented a good example of fracturing events in Fig. 12, which is the micro-seismic captured from simultaneously fractured well. Simulated reservoir volume (SRV) derived from microseismic data could be a great view to assistant reservoir modeling including fractures and supply a good evaluation on the fractures performance.

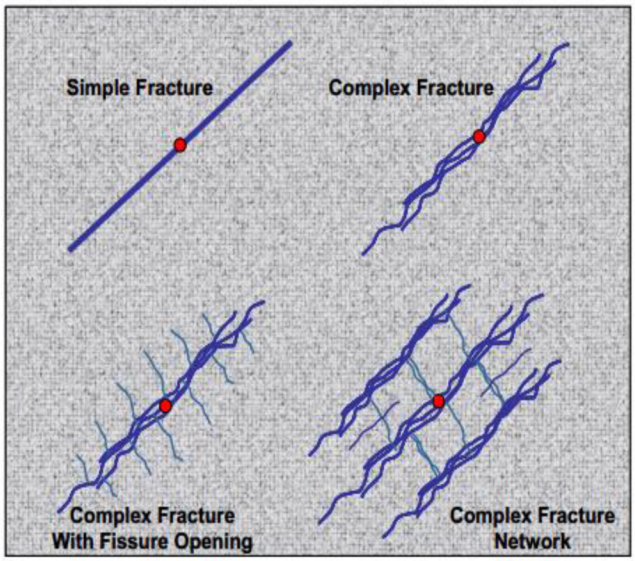

Figure 11—Types of fractures growth (Warpinski et al. 2008).

So far, we have built the 2D micro and macro models to exactly show how does nanoparticle flow along with two phase into shale reservoir and the changing trend of water saturation and mass concentration of nanoparticles. Taking into account that both the hydraulic fracture and complex fracture network need to be characterized in our reservoir model, a stimulated reservoir area (SRV) has been selected to represent the fractured shale reservoir in our model as Fig. 13. The SRV contains four various pore systems, where blue grids stand for well bore, red grids represent hydraulic fractures, light green denotes natural fractures, and the rest of white girds are shale matrix. Based on the conclusion obtained from the previous 2D models that nanoparticles and water are quite limited to flow into the organic matter, the matrix only contains non-organic matter in this large reservoir model. In our model, gas and water are only flowing into the wellbore through the hydraulic fractures and no direct connections between shale matrix and wellbore exist. Shale matrix (non-organic matter) has directly connections with natural fractures and hydraulic fractures, but water and gas have to flow into the natural fractures firstly and then enter the hydraulic fractures for most non-organic grids. Moreover, the well bore acting as the supplier of nanoparticles has higher water saturation and higher concentration of nanoparticles, while the shale matrix including natural fractures hold higher pressure than the hydraulic fractures and wellbore.

Table 2 shows the main initial parameters of the stimulated reservoir volume used in this simulator. Each of various grid has different size in X and Y axis, while they have same size in Z axis, 0.01 *m*. For example, the size of natural fracture grids on X and Y axes are 0.01 *and* 0.01/1.0 *m*. The porosity of inorganic matter is only 0.02 and the all others media have the porosity 1.0. From the wellbore to hydraulic fracture to natural fracture to inorganic matter, the permeability of these media decreases. The water saturation of natural fracture is 0.4 which means lots of gas exists. The water saturation of inorganic matter is 0.21, which is almost equal to its irreducible water saturation. Same with previous numerical models, this large reservoir model is also performed in isothermal condition, so we don't need worry about the heat and energy loss and transfer.

As the Table 2 and Fig. 13 show, the reservoir model includes the inorganic matter and natural fractures, hydraulic fractures, and wellbore system, and each media has different properties and parameter value at the initial condition. Fig. 14 shows the distribution of grid pressure and water saturation at the initial condition. On the left graph of Fig. 14, the horizontal red grids represent wellbore, and the four vertical grids stand for hydraulic fractures, and the rest of grids are shale matrix including inorganic matter and natural fractures. The numbers on the X and Y axes are the grid numbers: X axis is from grid one to grid forty seven, and Y axis is from grid one to grid thirty nine. Based on the Table 2, the right graph of Fig. 14 displays the distribution of water saturation for the entire reservoir, where you could see the inorganic grids (maroon color) are just like small islands separately isolated among the natural and hydraulic fractures in the stimulated reservoir zone.

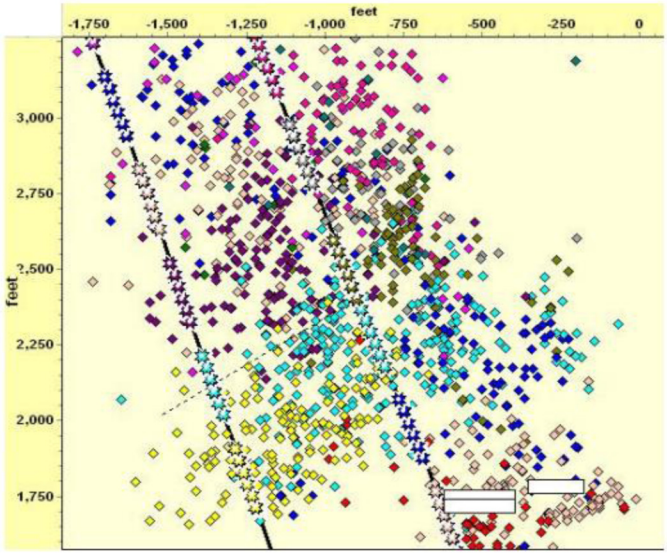

Figure 12—Microseismic record of fracturing events (King et al. 2008).

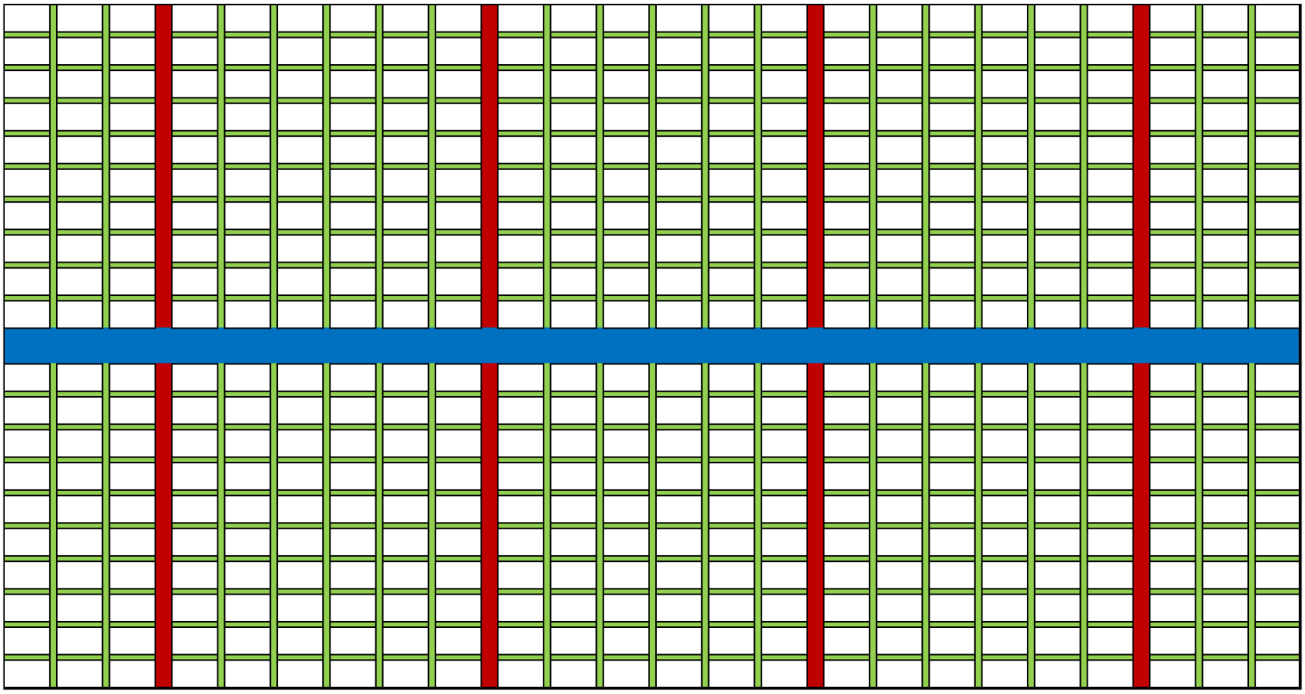

Figure 13—A sketch of multiple hydraulic fractured horizontal shale gas well.

The shale matrix including the non-organic grids and natural fractures has a higher initial pressure than the hydraulic fractures and well bore, which can results in the gas will flow out from the matrix into the hydraulic fractures. Meanwhile, water is acting as wetting phase in the non-organic matter, which leads to a lower flowing pressure of water phase because of capillary pressure effect. As the Fig. 3 shown, the capillary pressure is very high for water phase when the water saturation is about 0.21. What should be pointed out in Fig. 13 is that one pore media has more than one connections with another pore system, which will be explained as following. Most inorganic (non-organic matter) are only connected with natural fracture grids, while some are also directly connected with hydraulic fracture grids at the same time. For the natural fracture grids, they have connection with inorganic matter, natural fractures, and

Table 2—Initial parameters for stimulated reservoir volume

Initial Parameters for Stimulated Reservoir Volume					
Porosity Media		Inorganic	NF	HF	Wellbore
Size (m)		$1 \times 1 \times 0.1$	$1 \times 0.01 \times 0.1$	$1 \times 0.05 \times 0.1$	$1 \times 1 \times 0.1$
Porosity		0.02	1.0	1.0	1.0
Permeability		50 nD	84 mD	420 mD	8.4 D
Pressure (MPa)		27.2	27.2	4.0	4.0
Sw		0.21	0.4	0.99	0.99
Concentration (Kg/L)		1×10^{-20}	1×10^{-20}	1×10^{-20}	1×10^{-6}
Temperature (F)		100	100	100	100
Size (m)	X	1.0	0.01	0.05	1/0.01
	Y	1.0	1/0.01	1/0.01	1.0
	Z	0.1	0.1	0.1	0.1

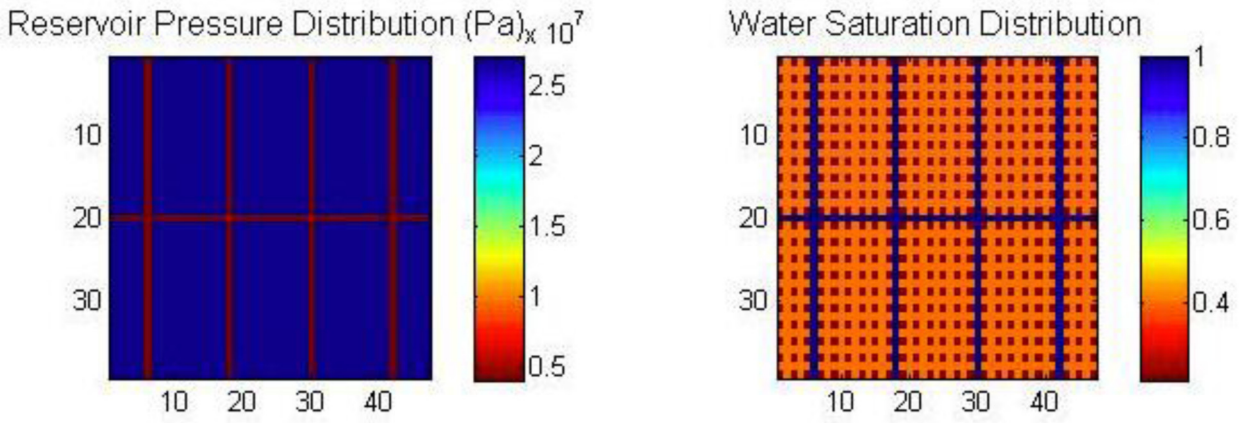

Figure 14—The distribution of pressure and water saturation at the initial condition.

themselves. Based on the difference of permeability, grid pressure, and other properties of these various pore systems, these different connections would bring various flow results. In the Fig. 15 below, the distributions of water saturation and nanoparticles mass are displayed at three different time steps: early, middle and final stages, where the exact time is also presented.

For the inorganic matter, gas is flowing out from the inorganic matter into the hydraulic fractures, and water is flowing from the hydraulic fractures and natural fractures into the inorganic matter. Due to water is wetting phase and a high capillary pressure exists for water phase in inorganic matter, so the natural fracture girds have a higher mobile water pressure than the inorganic grids. As a consequence, the pressure of inorganic matter decreases and its water saturation goes up. For the natural fracture grids without connection with hydraulic fractures, water is flowing out from them into the inorganic grid while gas is

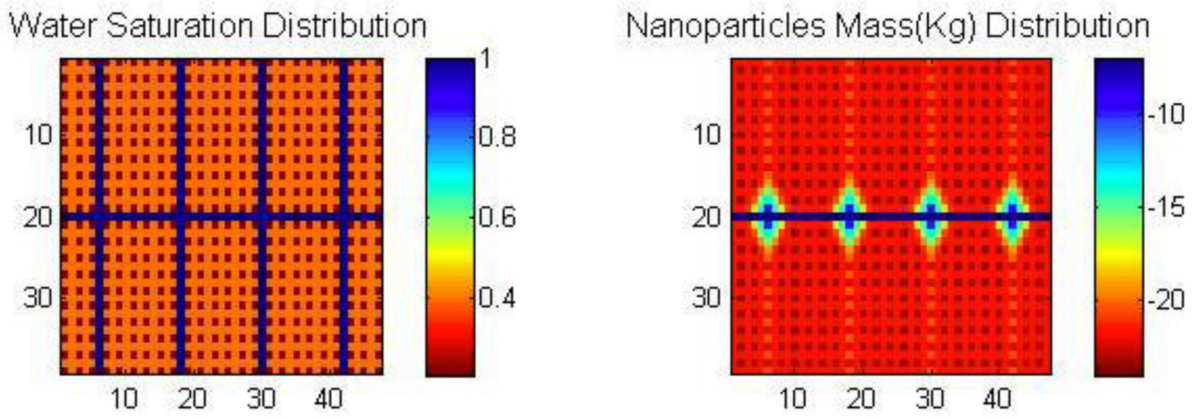

(a) Early time: t=5.02×10^1 s

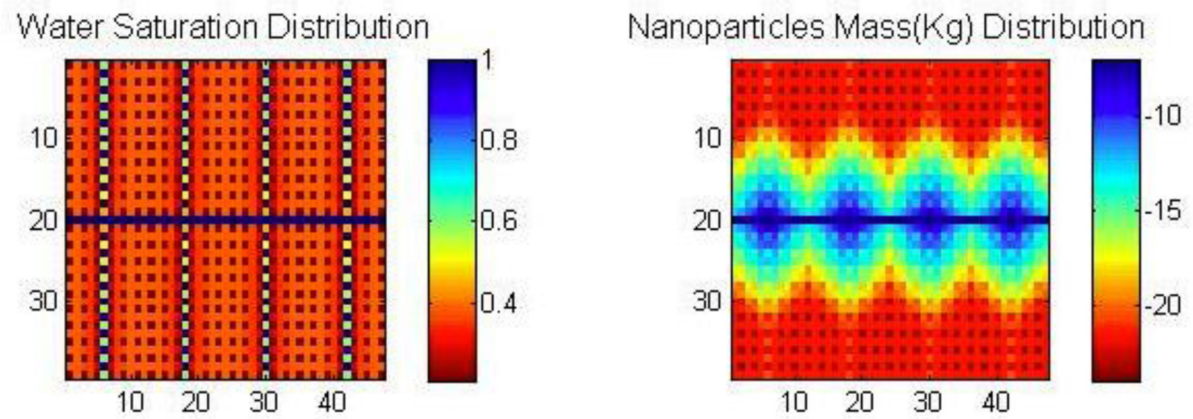

(b) Middle time: t=3.27×10^4 s

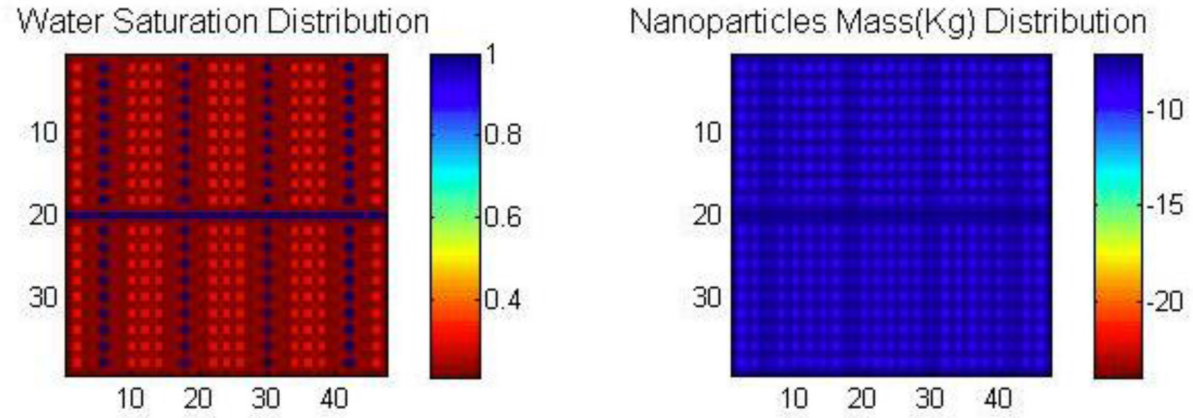

(c) Final time: t=2.5×10^9 s

Figure 15—The distribution of water saturation and nanoparticles concentration at different time steps in the Reservoir Model.

flowing from the inorganic matter into the natural fracture grids. For the natural fracture grids with connection with hydraulic fractures, water is flowing out from them into the hydraulic fractures because of high pressure gradient. As a results, the grid pressure rises and the water saturation decline for all the natural fracture grids. For the hydraulic fracture grids, there are two different types of connections: one is only connected with inorganic matter, and the other is only connected with natural fracture, so their changing trend of pressure, water saturating, and nanoparticle concentration is also different. For the hydraulic fracture grids connected with inorganic matter, numerous gas is flowing from the inorganic

grids into them while water is flowing in the inverse direction, which results in that the grid pressure keeps going up and water saturation keeps dropping in these hydraulic fracture grids. However, for these hydraulic fracture grids only connected with natural fractures, both of gas and water are flowing from the natural fracture grids into them, because capillary pressure effect is not considered in the natural fracture grids. So the grid pressure and water saturation of these hydraulic fractures keep increasing.

Fig. 15 (a) displays the distribution results about water saturation and nanoparticles concentration after 50.2 seconds. Due to wellbore acts as nanoparticles source, the water and nanoparticles start to flow from wellbore to hydraulic fractures and then to natural fractures and inorganic matter grids. Because of pressure difference, gas would flow out from the hydraulic fractures into the wellbore and then be produced, and the water phase including magnetic nanoparticles are gradually imbibed into the hydraulic fracture grids. You could clearly see the exact invasion phenomenon in the right graph of Fig. 15 (a). At the middle time stage of Fig. 15 (b), the dynamic process and results after the early time are presented, where more gas will flow out from the inorganic matter into the hydraulic fractures and well bore, and more and more nanoparticles and water are imbibed into the hydraulic fractures at the same time. Moreover, the nanoparticles are also flowing along the water phase into the natural fractures and inorganic matter girds further and further.

Fig. 15 (c) shows the final time step of the simulation after 2.5×10^9 seconds. The nanoparticles have spread into everywhere of the matrix and reached to a high level value. The pressure at the hydraulic fractures everywhere is about the same while the water saturation of hydraulic fractures varies depending on its location. The grids directly connected with the natural fractures keep a high value of water saturation, while the grids connected with the inorganic matter have a low value, which confirms what we have discussed above. Meanwhile, the water saturation of natural fractures is kind of higher than that of the inorganic matter girds while their pressure reach stable. In the right graph of Fig. 15 (c), the reason why the mass of nanoparticles is not equal everywhere is that the grids volume is different even though their nanoparticles concentration is very close. As Table 2, the inorganic grids is much larger than the hydraulic fracture grids, and the hydraulic fracture girds is five times bigger than the natural fracture girds. Consequently, the total mass of nanoparticles are dissimilar everywhere after multiplying the different grid volume as shown in Equation (10). In additional, the nanoparticles mass of wellbore is assumed to biggest and constant, so their value and color are never changed in the Fig. 15.

As the same with previous 2D models, the total mass of nanoparticles representing all the nanoparticles in the entire matrix is displayed along the time step in the Fig. 16. The nanoparticles mass could be computed by using Equation (10), which shows that the nanoparticles mass is related to nanoparticles concentration, water saturation, grid porosity, and grid volume. At the early stage, the total mass of nanoparticles does not rise quickly, because the water and nanoparticles just started to flow from the wellbore into the hydraulic fractures. When the time reach about 1.2×10^5 seconds, the growth rate significantly improves. After the time reaches about 1.0×10^8 seconds, the value of total nanoparticles approaches stable and keeps almost the same, which proves no more nanoparticles could flow into the reservoir matrix. Two important point could be obtained from this curve. One is when does the nanoparticles flow reach stable, and the other one is how much the nanoparticles can flow into the reservoir matrix. In this reservoir model, about 4.72×10^{-5} kilogram nanoparticles enter the stimulated reservoir volume. Of course, the total value will be certainly up to many different parameters, such as nanoparticles size and concentration, matrix structure, fractures pattern and fracture conductivity.

Magnetism Analysis

In this paper, synthesized Magnetic Carbon-Coated Iron-Oxide Nanoparticles is applied as the model nanoparticle example. Cooperating with Cheng and Dr. Heidari (2014), the iron oxide nanoparticles are produced by the reaction of hydrogen peroxide with ferrocene dissolved in acetone with the solvothermal chemical approach. Nuclear magnetic resonance (NMR) refers to the response of magnetic dipoles of

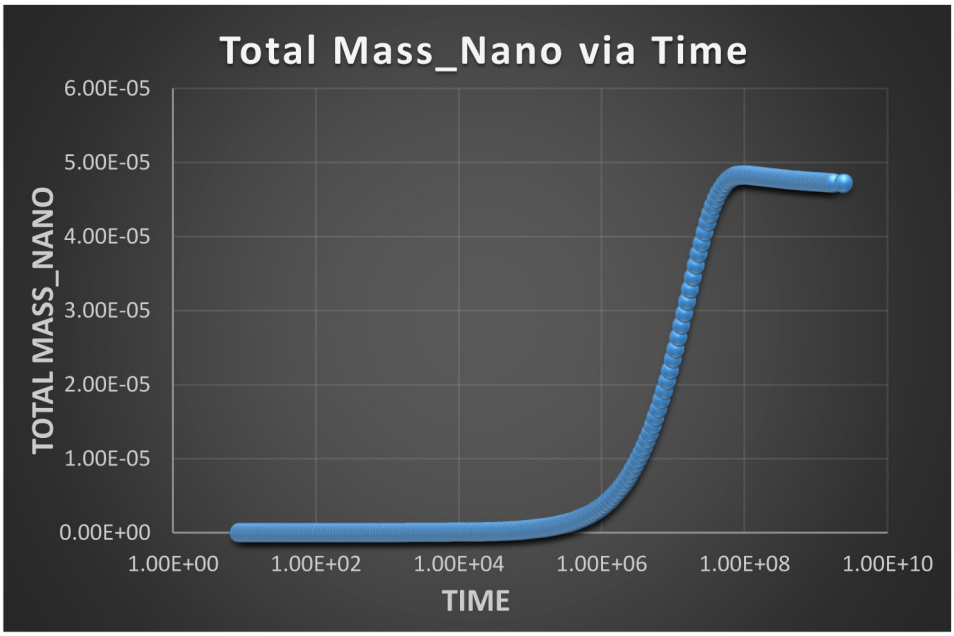

Figure 16—Total mass of nanoparticles at different time steps for reservoir model.

hydrogen nuclei in the presence of an applied magnetics field. The NMR technique can capture the magnetic signal which is released by hydrogen nuclei when they are return to their original state after an external magnetic field changed the position of atomic nucleus. As Equation (12) shows, Magnetic susceptibility is the degree to which a material can be magnetized in an external magnetic field. Since H is the applied external field, the magnetization of material is related to how strong the volume magnetic susceptibility is.

$$M = x_m \times H \tag{12}$$

Where M is magnetization of the material in amperes per meter, x_m is volume magnetic susceptibility, H is magnetic field strength in amperes per meter, the applied external field. Therefore, the total magnetization is made up of water, methane and magnetic nanoparticles in the shale reservoir as Equation (13). Additionally, the magnetic susceptibility of water and methane can be obtained from references. In our model, the value of magnetic susceptibility of water we used is 9.035×10^{-6} at 20°C, and the value of magnetic susceptibility of methane is 9.13×10^{-9} at 20°C. For a paramagnetic ion with non-interacting magnetic moments with angular momentum, the magnetic susceptibility is related with the individual ion's magnetic moments. The magnetic susceptibility of magnetic nanoparticles is calculated by using the Equation (14) and (15). Based on the previous results of the distribution of water saturation and nanoparticles concentration, the magnetic susceptibility could be easily computed through these equations.

$$M_{total} = (x_{m_{water}} + x_{m_{methane}} + x_{m_{nano}}) \times H \tag{13}$$

$$x_{m_{nano}} = \frac{N_A}{3k_BT}{\mu_{eff}}^2 = \frac{N_A}{3k_BT}{\mu_B}^2\left(\frac{\mu_{eff}}{\mu_B}\right)^2 \tag{14}$$

$$X_m = x_m \times \Phi \times S_i \times Vol_i \tag{15}$$

Where $x_{m_{water}}$ denotes the volume magnetic susceptibility of water, $x_{m_{methane}}$ indicates the volume magnetic susceptibility of methane, $x_{m_{nano}}$ stands for the volume magnetic susceptibility of magnetic nanoparticles, N_A is number of magnetic atoms per unit volume, k_B is Boltzmann's constant, T is absolute

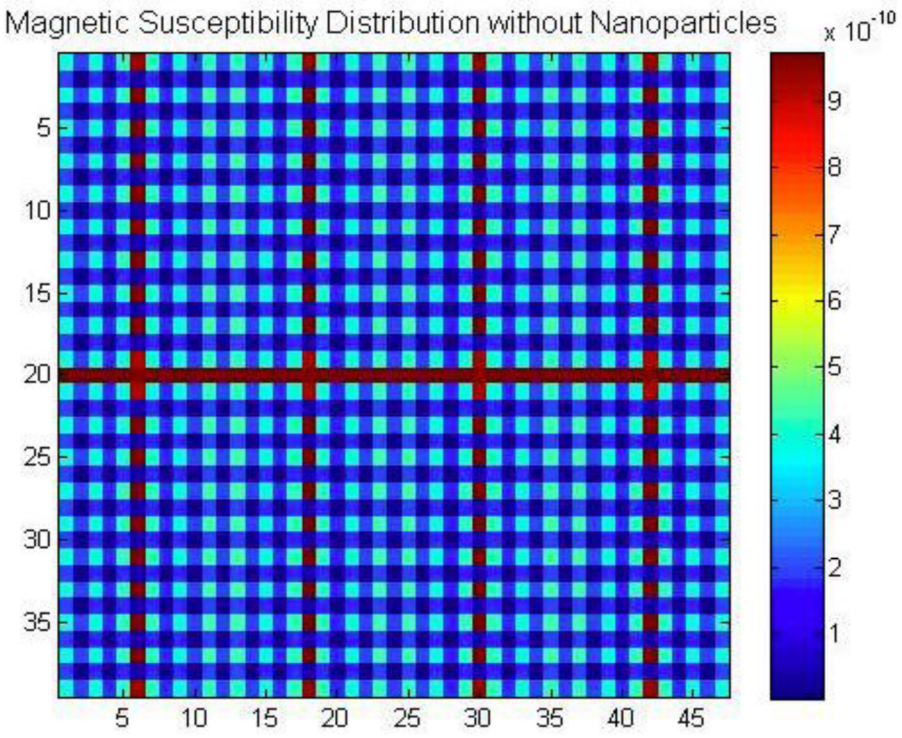

Figure 17—The distribution of magnetic susceptibility without magnetism from nanoparticles for the reservoir model.

temperature in kelvins, μ_{eff} is the effective magnetic moment per paramagnetic ion, μ_B is the Bohr magneton, X_m is magnetic susceptibility, ϕ is porosity of each grid, S_i is saturation of water or gas in grid, Vol_i is the volume of grid i.

Based on the magnetism theory and equations above, the distribution of magnetic susceptibility and total magnetization of reservoir could be computed for the shale reservoir. As the same reservoir matrix with the Fig. 13, two numerical cases are conducted and the results about the distribution of volume magnetic susceptibility are also shown in Fig. 17 and 18. One case does consider magnetic property for nanoparticle, and the other case does not. As we known, the magnetic nanoparticles are supposed to provide one more source for the volume magnetic susceptibility. As proved in the Fig. 17 and 18, even though both graphs look almost the same, while they have different value range. The numerical case considering magnetism for nanoparticles clearly possesses higher value of magnetic susceptibility among the entire fractured reservoir than the model without magnetism, which supports and proves the potential of magnetic nanoparticle enhancing the NMR logging signal. In the Fig. 17 and 18, the value of magnetic susceptibility is different in various pores media because of different grid volume. The value of magnetic susceptibility in natural fractures grids is less than that of inorganic grids, because their volume is much smaller than the grid volume of inorganic grids even though the natural fractures have higher water saturation and higher nanoparticle concentration. However, the value of magnetic susceptibility in hydraulic fractures is much larger than inorganic girds, because the hydraulic fractures have higher water saturation and nanoparticle concentration and also their grid volume is not too small compared to inorganic grids. To be clear, the volume magnetic susceptibility in hydraulic and natural fractures is higher than that of inorganic matter, so the final magnetization of these fractures should be definitely larger than that of inorganic matter grids.

To specific explore the influence of magnetic nanoparticles on the magnetic susceptibility, the fifth layer (from up to down) of SRV in Fig. 13 is chosen to show the total magnetic susceptibility in various media. As same with above, two numerical examples are performed and the results about magnetic

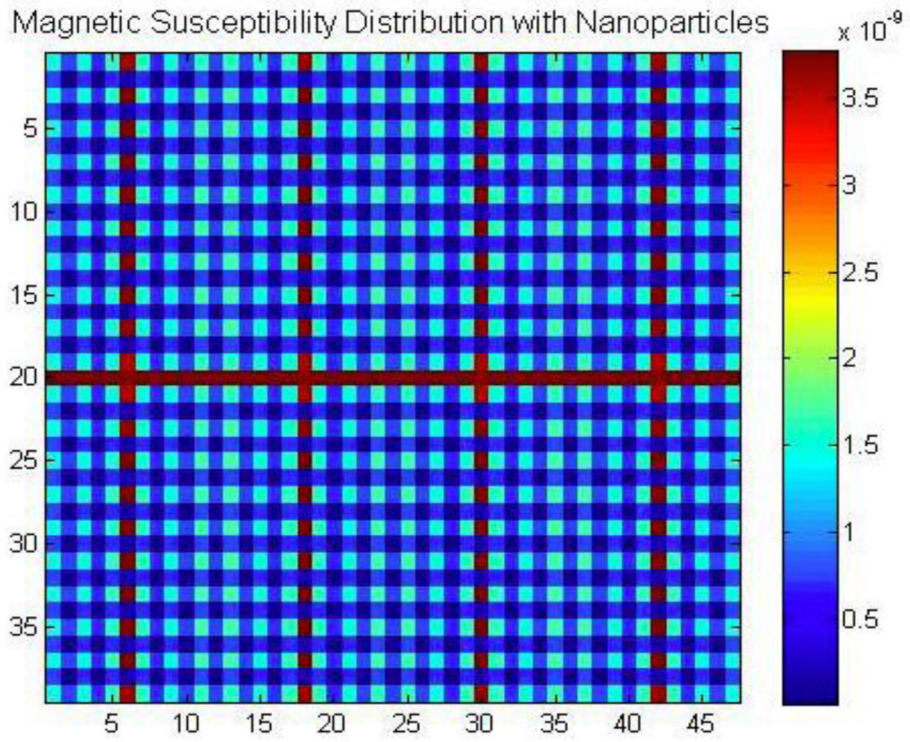

Figure 18—The distribution of magnetic susceptibility with magnetism from nanoparticles for the reservoir model.

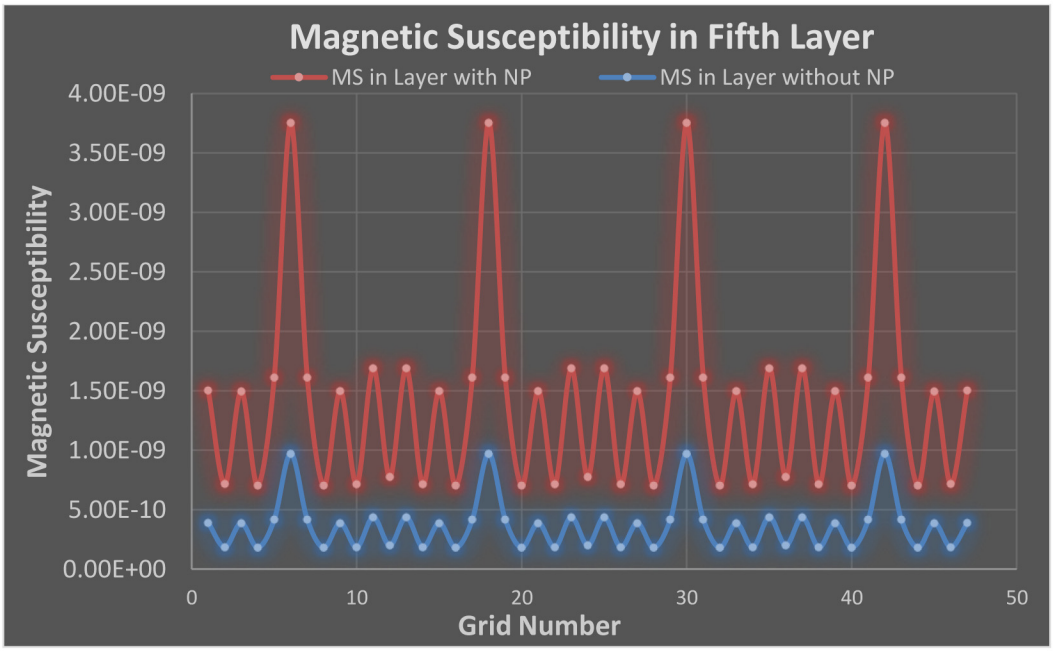

Figure 19—Magnetic susceptibility with and without Magnetism from nanoparticles in fifth layer of reservoir model.

susceptibility are also shown. The first case does not consider magnetism for nanoparticles and the total magnetic susceptibility are comprised of water and methane, as the blue curve in Fig. 19. The second case does take into account the magnetism for nanoparticles, so the total magnetic susceptibility is from magnetic nanoparticles, water, and methane, as the red curve in Fig. 19. In both cases of Fig. 19, the value of magnetic susceptibility is biggest in the hydraulic fracture grids and smallest in these natural fracture grids, and the reason is the same with what we have explained above.

Aderibigbe et al. (2014) have conducted some magnetic susceptibility experiments to investigate the influences of magnetic nanoparticles. In their experiment, several small liquid holders are built and horizontally placed, where simple water and water with nanoparticles are alternately stored into the single liquid holder. The value of magnetic susceptibility of each holder is measured and analyzed. Their results showed that the liquid holder containing magnetic nanoparticles obviously has higher MSL (magnetic susceptibility loop) unit than that of holder without magnetic nanoparticles. In addition, the ratio of magnetic susceptibility of the holder with magnetic nanoparticles to the holder without nanoparticles is about three to four, which is very close to our numerical model results of about 3.5. The experiment results from Aderibigbe et al confirms our numerical results, which in return provides more confidence to apply magnetic nanoparticles for producing enhanced signals for NMR logging devices.

Conclusions

This paper has developed a mathematical model looking at the nanoparticle transport in shale reservoirs; the model divides the reservoir into inorganic matter, organic matter, and fractures. Considering various flow mechanisms including Brownian diffusion, gas diffusion and desorption, Darcy flow, slippage flow, and capillary pressure effects and their application to specific sub-media, this stimulator provides a solid description for modeling dynamic flow of gas, water and nanoparticles in organic fractured shale reservoirs. 2D micro models were built to present the exact process of water and nanoparticles flowing into the matrix, then 2D macro models were created to display that how far these particles could flow into the matrix. A reservoir model containing stimulated reservoir volume was subsequently built to show the changing trend of water saturation and nanoparticle concentration at reservoir scale. Based on the diverse sources of magnetism, the distribution of magnetic susceptibility and magnetization of the reservoir was computed and presented. Similar results were obtained and compared with each other from the same reservoir models with and without considering magnetism for nanoparticles. In addition, the results of the distribution of magnetic susceptibility were compared with some experimental data to validate the model's accuracy and predictability. Overall, seven main conclusions are shown as following:

1. The mathematic model considering sub-divided pores media, various flow mechanisms, and mixed wettability is developed to describe the nanoparticles transport carried by a two-phase flow in shale reservoirs.
2. Nanoparticles can easily flow along fractures, whereas their transport into shale matrix is limited, only about 20 centimeters on our models, especially restricted for organic matter.
3. Brownian diffusion contributes about 18% of the transport of a nanoparticle, which means Darcy flow is the major flow contributor.
4. Refining the mesh provides almost the same results on mass accumulation of nanoparticles which confirms the accurate computation of the models.
5. The magnitude of magnetic susceptibility is related to the permeability, water saturation and volume of pore media.
6. The magnetic nanoparticles effectively enlarge the magnetic susceptibility of reservoirs.
7. The numerical results are compared with and confirmed by the experimental results from Aderibigbe et al., which provides more confidence to apply magnetic nanoparticles for producing enhanced signals from NMR logging devices.

Acknowledgements

The author would like to thank The Crisman Institute at Texas A&M University for funding this project. Special thanks to my supervisor Dr. John Killough for his excellent technique guidance and also thanks to Dr. Zoya Heidari for her support during this project.

Nomenclature

A_{nm} = Interface between grid m and n
D_e = Diffusion coefficient of nanoparticles
F_l = Flux of component l
F_{nm} = Average value of normal flux from grid m and n
K_B = Boltzmann constant
M_l = Mass accumulation of component l
M_{total} = Total magnetization of reservoir
N_A = Number of magnetic atoms per unit volume
N_{inorg} = Number of Inorganic matter in the mesh
N_{krg} = Number of Kerogen grids in the mesh
P_c = Capillary pressure
Q_{Nano} = Source and Sink of nanoparticles
Q_l = Source and Sink of component l
s_w = Water saturation
S_β = Saturation of phase β
V_n = Volume of grid block n
Vol_i = Volume of grid block i
X_m = Magnetic susceptibility
X_β^l = Mass fraction of component I in the phase β
d_p =Diameter of nanoparticles
$k_{r\beta}$ =Relative permeability to the phase β
m_{NPs} =Mass of nanoparticles
x_m = Volume magnetic susceptibility
M_B = Bohr magneton
μ_{eff} = Effective magnetic moment per paramagnetic ion
μ_w = Water saturation
μ_β = Viscosity of phase β
p_{inorg} = Density of Inorganic matter
p_{krg} = Density of Kerogen matter
p_β = Density of phase β
ϕ_{inorg} = Porosity of Inorganic matter
ϕ_{krg} = Porosity of Kerogen matter
Δt = Time step size
EIA = Energy Information Administration
NMR = Nuclear Magnetic Resonance
SEM = Scanning Electron Microscope
SRV = Stimulated Reservoir Volume
TOC = Total Organic Carbon
C = Concentration of nanoparticles
D = Dimension
F = Flux of component
H = Magnetic field strength
MSL = Magnetic Susceptibility Loop
NPs = Nanoparticles
P = Pressure
Q = Source and Sink of component

R = Residual
T = Absolute temperature
b = Klinkenberg factor
g = Gravitational acceleration vector
k = Absolute permeability of porous media
I = Index of component
mD = Millidarcy
nD = Nanodarcy
t = Time
Φ = Porosity of pore media
β = Index of phase
ϕ = Porosity of porous media

References

Aderibigbe, A., Cheng, K., Heidari, Z., Killough, J., Texas A&M University, Fuss, T., and Stephens, W. T., Saint-Gobain Proppants. 2014. Detection of Propping Agents in Fractures using Magnetic Susceptibility Measurements Enhanced by Magnetic Nanoparticles. Paper prepared for presentation at the SPE Annual Technical Conference and Exhibition, Amsterdam, The Netherlands, Oct. 27-29.

Alfi, M., Yan, B., Cao, Y. et al. Three-Phase Flow Simulation in Ultra-Low Permeability Organic Shale Via a Multiple Permeability Approach. *Society of Petroleum Engineers*. DOI: 10.15530/urtec-2014-1895733.

Alfi, M., Yan, B., Cao, Y., An, C. et al. 2014. How to Improve our Understanding of Gas and Oil Production Mechanisms in Liquid-rich Shale. Paper prepared for presentation at the SPE Annual Technical Conference and Exhibition, Amsterdam, The Netherlands, Oct. 27-29.

Ambrose, R.J., Hartman, R.C., Diaz Campos, M. et al. New Pore-Scale Considerations for Shale Gas in Place Calculations. *Society of Petroleum Engineers*. DOI: 10.2118/131772-MS.

Ambrose, R.J., Hartman, R.C., Diaz Campos, M. et al., 2010, New Pore-Scale Considerations for Shale Gas in Place Calculations. *Society of Petroleum Engineers*. DOI: 10.2118/131772-MS.

Bartko, K., Salim, A., Saldungaray, P. et al. Hydraulic Fracture Geometry Evaluation Using Proppant Detection: Experiences in Saudi Arabia. *Society of Petroleum Engineers*. DOI: 10.2118/168094-MS.

Cheng, K., Aderibigbe, A., Alfi, M., Heidari, Z., and Killough, J., 2014, Quantifying the impact petrophysical properties on spatial distribution of contrasting nanoparticle agents: Paper presented at the SPWLA 55th Annual Logging Symposium, Abu Dhabi, United Arab Emirates, May 18-22.

Cipolla, C.L., Lolon, E., Erdle, J.C. et al. Reservoir Modeling in Shale-Gas Reservoirs. *Society of Petroleum Engineers*. DOI: 10.2118/125530-MS.

Civan, F., Rai, C. S., Sondergeld, C. H. 2011. Shale-gas Permeability and Diffusivity Inferred by Improved Formulation of Relevant Retention and Transport Mechanisms, Transport in Porous Media, Vol. **86**(3): 925–944.

Curtis, M. E., Sondergeld C. H., Ambrose, R. J., Rai, C. S. 2012. Microstructural investigation of gas shales in two and three dimensions using nanometer-scale resolution imaging, *AAPG Bulletin,* **96,** p.665–677.

Curtis, M.E., Ambrose, R.J., and Sondergeld, C.H., 2010, Structural Characterization of Gas Shales on the Micro- and Nano-Scales. *Society of Petroleum Engineers*. DOI: 10.2118/137693-MS.

El-amin, M.F., Salama, A., and Sun, S., 2012, Modeling and Simulation of Nanoparticle Transport in a Two-Phase Flow in Porous Media. *Society of Petroleum Engineers*. DOI: 10.2118/154972-MS.

El-Amin, M.F., Sun, S., and Salama, A., 2012, *Modeling and Simulation of Nanoparticle Transport*

in Multiphase Flows in Porous Media: Co2 Sequestration.

Elimelech, M. and O'Melia, C.R. 1990. Kinetics of Deposition of Colloidal Particles in Porous Media. *Environmental Science & Technology* **24**(10): 1528–1536). DOI: 10.1021/es00080a012

Energy Information Administration (EIA). 2013. *Annual Energy Outlook Report 2013,* http://www.e-ia.gov/forecasts/aeo/pdf/0383(2013).pdf.

Fisher, M.K., Heinze, J.R., Harris, C.D. et al., 2004, Optimizing Horizontal Completion Techniques in the Barnett Shale Using Microseismic Fracture Mapping. *Society of Petroleum Engineers*. DOI: 10.2118/90051-MS.

Javadpour, F., Nanopores and Apparent Permeability of Gas Flow in Mudrocks (Shales and Siltstone). 2009. J. of Canadian Petroleum Tech., V. **48,** pp 16–21.

Ju, B. and Fan, T. 2009. Experimental Study and Mathematical Model of Nanoparticle Transport in Porous Media. *Powder Technology* **192**(2): 195–202). DOI: http://dx.doi.org/10.1016/j.pow-tec.2008.12.017

Killough, J.E., Wang, Y., and Yan, B. Beyond Dual-Porosity Modeling for the Simulation of Complex Flow Mechanisms in Shale Reservoirs. *Society of Petroleum Engineers*. DOI: 10.2118/163651-MS.

King, G.E., Haile, L., Shuss, J.A. et al., 2008, Increasing Fracture Path Complexity and Controlling Downward Fracture Growth in the Barnett Shale. *Society of Petroleum Engineers*. DOI: 10.2118/119896-MS.

Mayerhofer, M.J., Lolon, E., Warpinski, N.R. et al., 2010, What Is Stimulated Rock Volume? *Society of Petroleum Engineers*. DOI: 10.2118/119890-MS.

Millington, R. J. and J. M. Quirk, 1961. Permeability of porous solids. *Trans. Faraday Soc.* **57**:1200–1207.

Sbai, M.A. and Azaroual, M. 2011. Numerical Modeling of Formation Damage by Two-Phase Particulate Transport Processes during Co2 Injection in Deep Heterogeneous Porous Media. *Advances in Water Resources* **34**(1): 62–82). DOI: http://dx.doi.org/10.1016/j.advwa-tres.2010.09.009

Shabro, V., Torres-Verdin, C., and Sepehrnoori, K., 2012, Forecasting Gas Production in Organic Shale with the Combined Numerical Simulation of Gas Diffusion in Kerogen, Langmuir Desorp-tion from Kerogen Surfaces, and Advection in Nanopores. *Society of Petroleum Engineers*. DOI: 10.2118/159250-MS.

Swami, V. and Settari, A. A Pore Scale Gas Flow Model for Shale Gas Reservoir. *Society of Petroleum Engineers*. DOI: 10.2118/155756-MS.

Swami, V. *Shale Gas Reservoir Modeling: From Nanopores to Laboratory*.

Wang, F.P. and Reed, R.M. Pore Networks and Fluid Flow in Gas Shales. *Society of Petroleum Engineers*. DOI: 10.2118/124253-MS.

Warpinski, N.R., Mayerhofer, M.J., and Vincent, M.C. et al. Stimulating Unconventional Reservoirs: Maximizing Network Growth While Optimizing Fracture Conductivity. *Society of Petroleum Engineers*. DOI: 10.2118/114173-MS.

Wu, Y. S. and Pruess, K., 2000, Numerical Simulation of Non-isothermal Multiphase Tracer Transport in Heterogeneous Fractured Porous Media: *Advances in Water Resources,* Vol.**23,** pp. 699–723.

Yan, B., Alfi, M., Wang, Y. et al. A New Approach for the Simulation of Fluid Flow in Unconven-tional Reservoirs through Multiple Permeability Modeling. *Society of Petroleum Engineers*. DOI: 10.2118/166173-MS.

Yan, B., Killough, J.E., Wang, Y. et al. Novel Approaches for the Simulation of Unconventional Reservoirs. *Society of Petroleum Engineers*. DOI: 10.1190/URTEC2013-131.

Yu, J., Berlin, J.M., Lu, W. et al. *Transport Study of Nanoparticles for Oilfield Application*.

Yu, W. and Sepehrnoori, K. Optimization of Multiple Hydraulically Fractured Horizontal Wells in Unconventional Gas Reservoirs. *Society of Petroleum Engineers*. DOI: 10.2118/164509-MS.

Zhang, T., 2012, *Modeling of Nanoparticles Transport in Porous Media*: Ph.D. Dissertation, The University of Texas at Austin, USA.

Zhang, T., Ellis, G.S., Ruppel, S.C. et al. 2012. Effect of Organic-Matter Type and Thermal Maturity on Methane Adsorption in Shale-Gas Systems. *Organic Geochemistry* **47**(0): 120–131. DOI: http://dx.doi.org/10.1016/j.orggeochem.2012.03.012.